Morphological Dynamics-Based Anomaly Detection Towards In Situ Layer-Wise Certification for Directed Energy Deposition Processes

Mahathir Mohammad Bappy
Department of Industrial and Systems Engineering,
Mississippi State University,
Mississippi State, MS 39762
e-mail: mmb888@msstate.edu

Chenang Liu
School of Industrial Engineering and Management,
Oklahoma State University,
Stillwater, OK 74078
e-mail: chenang.liu@okstate.edu

Linkan Bian
Department of Industrial and Systems Engineering,
Center for Advanced Vehicular Systems,
Mississippi State University,
Mississippi State, MS 39762
e-mail: bian@ise.msstate.edu

Wenmeng Tian[1]
Department of Industrial and Systems Engineering,
Center for Advanced Vehicular Systems,
Mississippi State University,
Mississippi State, MS 39762
e-mail: tian@ise.msstate.edu

The process uncertainty induced quality issue remains the major challenge that hinders the wider adoption of additive manufacturing (AM) technology. The defects occurred significantly compromise structural integrity and mechanical properties of fabricated parts. Therefore, there is an urgent need in fast, yet reliable AM component certification. Most finite element analysis related methods characterize defects based on the thermomechanical relationships, which are computationally inefficient and cannot capture process uncertainty. In addition, there is a growing trend in data-driven approaches on characterizing the empirical relationships between thermal history and anomaly occurrences, which focus on modeling an individual image basis to identify local defects. Despite their effectiveness in local anomaly detection, these methods are quite cumbersome when applied to layer-wise anomaly detection. This paper proposes a novel in situ layer-wise anomaly detection method by analyzing the layer-by-layer morphological dynamics of melt pools and heat affected zones (HAZs). Specifically, the thermal images are first preprocessed based on the g-code to assure unified orientation. Subsequently, the melt pool and HAZ are segmented, and the global and morphological transition metrics are developed to characterize the morphological dynamics. New layer-wise features are extracted, and supervised machine learning methods are applied for layer-wise anomaly detection. The proposed method is validated using the directed energy deposition (DED) process, which demonstrates superior performance comparing with the benchmark methods. The average computational time is significantly shorter than the average build time, enabling in situ layer-wise certification and real-time process control. [DOI: 10.1115/1.4054805]

Keywords: additive manufacturing, anomaly detection, certification, directed energy deposition, morphological analysis, thermal history, inspection and quality control, rapid prototyping and solid freeform fabrication, sensing, monitoring and diagnostics

1 Introduction

The metal-based additive manufacturing (AM) technologies have demonstrated their significant potential by producing fully functional parts with reduced production time and costs for low-volume and high-value complex-shaped components. The AM technologies provide the opportunity to manufacture parts of diverse designs in both nonstandard and remote environments, which is not feasible for conventional manufacturing processes. Moreover, AM is also capable of reducing the overall time-to-market of new products by accelerating the in-house testing of the designed prototypes prior to first market introduction [1,2]. The directed energy deposition (DED) process is a widely used metal-based AM process with the capacity of product prototyping, production, and component repair. During the fabrication, the feedstock material is deposited while being melted and subsequently solidified on top of the previous layer to gradually form the final geometry [3]. The high uncertainty in the DED process may lead to quality issues in the final parts, including porosity, cracks, and lack of fusion [4]. These issues will significantly compromise the mechanical properties and reliability of the fabricated AM components, hindering broader adoption of DED technologies in various mission-critical applications. Therefore, there is an urgent need in developing reliable certification methods to accelerate the scale up of DED technologies [4,5].

AM component certification refers to evaluating the conformity of the component during or after the fabrication based on the preestablished standards [6]. In practice, AM component certification activities are essential to assure the trustworthiness and reliability of the AM components, especially for mission-critical applications [7]. To satisfy the needs for certification, various anomaly detection methods can provide critical information for AM component certification, where different inspection techniques can be adopted to identify and characterize the critical flaws (e.g., porosity and crack) in the fabricated component [8,9].

In the DED process, the thermal history is capable of characterizing process dynamics to predict material microstructure and its resulting mechanical properties. Various AM process modeling studies focus on characterizing process thermal history. Some approaches characterize the thermal history using finite element models (FEMs) [10,11]. However, they are usually extremely computationally expensive, highly dependent on the design geometry, and very cumbersome to capture process uncertainty [4]. Additionally, notable advancements of sensor technologies have enabled in situ monitoring and anomaly detection towards component certification for metal-based AM [4,12,13]. Most approaches for in situ AM process monitoring are performed through the feature extraction from thermal images [13–15]. Alternatively, the layer-wise

[1]Corresponding author.

Manuscript received March 6, 2022; final manuscript received June 7, 2022; published online July 26, 2022. Assoc. Editor: Qiang Huang.

thermal image series can capture the complete spatiotemporal information in a layer-wise manner, which is more robust for anomaly detection of the fabricated parts. However, in most studies, only local features extracted from individual thermal images are considered, and those approaches cannot be directly applied to layer-wise certification, and the key reasons include: (1) the thermal distribution of different layers varies continuously (i.e., mushroom effect), and thus it is difficult to establish one benchmark distribution for all the layers in one build [4]; (2) given a complicated component, the thermal behavior also varies as a function of the printing path, which needs to be accounted for in the anomaly detection method [16]; and (3) the state-of-the-art approaches are usually purely data-driven and thus do not directly quantify the morphological dynamics of melt pools [17,18], which often makes their anomaly detection models and results challenging to interpret.

To fill these gaps, a new in situ layer-wise AM anomaly detection method is proposed by characterizing the morphological dynamics of the melt pools and heat affected zones (HAZs) which are segmented based on specific temperature ranges. In this study, the optimal transport problems are leveraged to formulate the morphological dynamics, and a new Wasserstein distance (WD)-based transition metric system is developed to characterize the temporal variation in the melt pool and HAZ morphologies, respectively. Subsequently, several new layer-wise key process features are extracted and used for layer-wise anomaly detection, facilitated by a supervised machine learning framework.

The *technical contributions* of this paper are summarized as follows. First, it explicitly establishes a physics-informed formulation of layer-wise melt pool and HAZ morphology dynamics to characterize the stability of thermal history. Second, several novel layer-wise process key features are proposed for the layer-wise anomaly detection of the DED process based on the melt pool and HAZ transition metrics with validated better performance than the state-of-the-art approaches, providing critical information towards AM component certification. The impacts to the research community and industries are twofold. For the AM quality control area, the newly proposed method opens the new venue of physics-informed data-driven anomaly detection for AM processes, which provides critical information for component-wise certification as well as guiding in situ process control practices for AM quality improvement. For AM industrial practices, reliable layer-wise anomaly detection can significantly reduce the needs for post-manufacturing inspection for AM components certification and ultimately accelerate the broader adoption of AM technologies in mission-critical applications.

The remainder of the paper is organized as follows. A literature review on the state-of-the-art metal-based AM process anomaly detection techniques is summarized in Sec. 2. The proposed methodology for developing the new melt pool and HAZ transition metrics and their properties, and layer-wise certification are introduced in Sec. 3. In Sec. 4, case studies of fabricating a thin wall and a cylindrical specimen using the DED process are presented, and the performance of the proposed method is compared with the benchmark methods. Finally, Sec. 5 presents the conclusion and potential future research directions.

2 Literature Review

This section briefly summarizes the state-of-the-art methodologies for metal-based AM process anomaly detection. The major metrological technologies used for AM anomaly detection are first summarized. Subsequently, the defect characterization and modeling techniques based upon the data collected using the metrological technologies are summarized. Lastly, the research gaps of machine learning-based AM anomaly detection are briefly discussed.

2.1 Metrological Techniques for Additive Manufacturing Anomaly Detection. Most data-driven AM anomaly characterization methods heavily rely on data collected from the metrological techniques used. In this section, a comprehensive review and comparison among different metrological techniques used for AM quality assurance and certification is conducted. The respective merits and limitations of the most widely used metrological approaches are briefly summarized in Table 1.

All the metrological techniques can be briefly categorized into two types, in situ and post-manufacturing techniques (as illustrated

Table 1 Comparison of different metrological techniques

Approach	Data description	Merits	Limitations	Inspection type
XCT	The XCT generates 3D images of a specimen by combining cross-sectional image of the object to represent internal structure non-destructively [19,20]	• Characterizes internal defects and structure of the object • Generates 3D voxel geometry based on 2D radial slices [19]	• Time intensive and costly [20] • Limited size of the inspected parts • Require high capacity computer data storage [19]	Post-manufacturing
MRI	The MRI captures the cross-sectional image of the structure [21]	• Performs scanning without radiation • Suitable for soft structure [21]	• Very expensive • Requires enclosed space due to loud noise [20]	Post-manufacturing
UT	UT generates phase velocity to measure flaws in the test specimen [22]	• Unhazardous process [20]	• Expensive technique • Specimen surface needs to be accessible and smooth [22]	Post-manufacturing
Pyrometer	Pyrometer captures in situ temperature profile as a thermal image [12]	• Non-contact method • Suitable for thermal hazardous environments [20]	• Noise affects measurement efficiency • Loss of thermal radiation spectrum [20]	In situ
IR camera	It uses infrared and the visual region to produce image of the object [20]	• Captures thermal information with images [20]	• Range of emissivity and reflection affects accuracy [20]	In situ
High-speed camera	It captures images of high-speed processes [20]	• Very high image capture rate [20]	• Lens distortion and non-alignment of sensor generate erratic image [20]	In situ
3D Scanner	It collects point clouds—a type of high-density data in 3D coordinate systems in a fast and reliable manner [23,24]	• More sensitive to geometric variations of object [23]	• Only captures the morphological information of the scanned object [23]	In situ

in Table 1). In cases of in situ sensing technologies, the measurements are taken from the system without interrupting or hampering the AM process. The post-manufacturing inspection technologies, on the other hand, can only be used after the completion of the part fabrication. Therefore, those in situ metrological techniques can be used to develop real-time process monitoring and quality prediction models, and the post-manufacturing approaches can be used to provide the validation for those data-driven models.

2.2 Post-Manufacturing Anomaly Characterization. The defect characterization methods, including X-ray computed topography (XCT), magnetic resonance imaging (MRI), and ultrasonic testing (UT), are widely used for post-manufacturing anomaly characterization of AM parts [3–5]. The XCT technique is used in metal-based AM to measure porosity occurrences, their spatial distribution, and severity in the build parts [12,25]. The XCT data can be analyzed using the computer aided quality technology to trace the porosity orientation in the printed parts [26]. Moreover, the XCT can be analyzed using machine learning tools for automatic segmentation of porosity from the scanned images of metallic specimens [27]. Compared to other post-manufacturing methods, XCT can provide detailed 3D information even for complex geometries. However, the XCT process usually requires high energy and skilled operators to operate the machine. In addition, the XCT machine is subject to high capital cost, and the inspection process is extremely time consuming [20].

MRI is used to track the overall structure of the AM parts using radio frequency pulses and powerful magnetic field [21]. The MRI systems can produce the cross-sectional images of the structures by capturing magnetic field intensity gradient without ionizing radiation as observed in XCT scans [20,21]. However, in this approach, a complex shape may need to be tested for multiple times to obtain precise structural information, making it time consuming and complicated in data collection [20].

The UT technology is also primarily used to characterize the internal structure of parts [28]. Basically, the ultrasonic phase velocity is used to characterize the defects like pores and voids in AM parts. In some studies, during experimentation, the samples are printed with a porosity of up to 5–15%, and the output denotes that the measured phase velocity is inversely proportional to porosity [22,29]. Moreover, the ultrasonic phase velocity can characterize defects and microstructures of AM parts. For example, changing process parameters, like hatch spacing and mechanical properties, can affect the defect formation, leading to varying pores numbers, sizes, and shapes, which can be captured by the UT technology [22]. As a nondestructive technique, UT measurements can be integrated with other monitoring techniques for developing a comprehensive evaluation system for AM parts. It is very important to maintain standard experimental procedures including voltage gain, pulse repetition frequency, and good surface finish, otherwise few degrees of change can deviate important signal information [29].

In summary, although the post-manufacturing approaches generate good information about the internal structure and surface properties of the AM parts, they are extremely high skill demanding, time consuming, and costly in nature [4,20]. Therefore, it is challenging and usually impractical to extensively apply these post-manufacturing technologies in AM certification. However, the detailed information and superior accuracy of post-manufacturing approaches make them a good choice for providing limited labeling information for supervised and/or semi-supervised learning for in situ AM certification.

2.3 In Situ Anomaly Detection and Process Monitoring Based on Image Analysis. In situ monitoring of the AM process can capture the process uncertainty and thus can certify the AM process/part in real time. For in situ AM process monitoring and anomaly detection, multiple data sources of thermal imaging, optical imaging, and 3D scanning can be used to capture the process information during the fabrication of AM parts. In this section, the recent works in anomaly detection are categorized based on the sensing technologies used, namely, thermal imaging, video streams, and 3D point cloud.

The thermal characteristics are identified as one of the most informative process signals for the AM process dynamics. During the fabrication of AM parts, the thermal history can be used for process monitoring, microstructural assessment, and mechanical properties prediction [30]. In general, the AM process thermal history is captured as a high-resolution thermal image stream, which are subsequently used for developing data-driven approaches to model process dynamics for anomaly detection [12,31–33]. In the specific case of metal-based AM, major proportion of the published works are conducted with thermal imaging systems, where the machine learning-based models are developed for in situ anomaly detection. In some studies, along with the thermal history, the morphological features of the melt pool (e.g., depth, size, and temperature distribution) are extracted for anomaly detection [11,12,14]. Furthermore, instantaneous temperatures, melt pool orientations, and aspect ratios are also estimated based on pyrometry observation for defect detection [34]. Besides these, tensor decomposition has been applied to the thermal images for dimension reduction, making it easy to model the process-defect relationship [4]. In addition, deep learning-based models are developed to link the layer-wise images and the ground truth XCT data for autonomous anomaly detection and classification [35,36]. Moreover, unsupervised anomaly detection method based on neural networks is also used for distance-based multivariate anomaly detection [37]. With only a few exceptions of layer-wise modeling proposed by Seifi et al. [4] and Esfahani et al. [16], most of the existing data-driven approaches focus on process monitoring and anomaly detection only considering individual thermal images, which fails to characterize layer-wise process condition and part quality. However, quantifying the morphological variability of the multiple melt pools within a layer will provide a new process knowledge-driven approach for anomaly detection.

Another stream of research utilizes the in situ optical video acquisition technique, which has become more accessible due to the availability of robust machine vision systems integrated with the AM process, enabling highly efficient online anomaly detection and process monitoring [38–40]. Using the video as a spatiotemporal data stream, the integrated spatiotemporal decomposition and regression-based modeling is proposed for in situ anomaly detection and monitoring [41]. In addition, this method can be applied to any image-based process monitoring applications where the foreground events are random and sparse, and the anomaly is spatially and temporally correlated. A recursive estimation procedure for real-time implementation of the algorithm is also proposed to handle the challenges of the high dimensionality of the video-image stream. However, the spatial information of the video streams may not be sufficient to distinguish the anomalous events from other natural foreground [41,42].

Three-dimensional point cloud data are used for geometric deviation and surface defect detection of AM parts [23,43]. The machine learning models can be trained with synthetic 3D point clouds rather than experimental data that can reduce training time and costs associated with many prints for each design [44]. Basically, 3D point clouds are high-density data and used to measure the geometric integrity of the AM products fabricated through a variety of processes. Specifically, dimensional or surface variation induced by miniature process shifts in the AM system can be detected and characterized using point cloud-based approaches [23]. For instance, the laser-scanned 3D point cloud data are used for identifying dimensional variation in AM parts [45]. Although the point clouds data are more capable of depicting structural information of the printed parts compared to low-dimensional signals, translating the 3D point clouds data into a model is very difficult due to the computational complexity and segmentation precision issues [45,46].

2.4 Discussion of Research Gaps. This section discusses the research gaps in the state-of-the-art machine learning-based

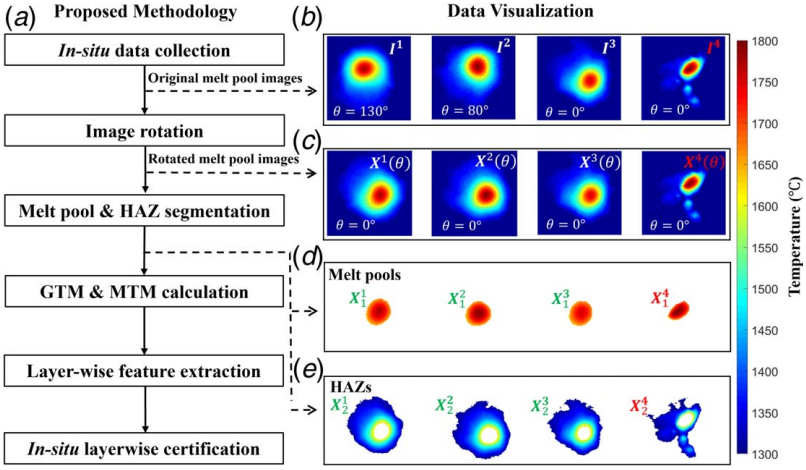

Fig. 1 The proposed method of in situ layer-wise anomaly detection by characterizing morphology dynamics of melt pools and HAZs: (*a*) overall proposed methodology, (*b*) original melt pool images, (*c*) rotated melt pool images, (*d*) melt pools, and (*e*) heat affected zones

anomaly detection methods for anomaly detection of metal-based AM processes.

The machine learning models aim to capture the process-defect relationships to distinguish between anomaly inducing samples and healthy samples, with various machine learning models being adopted [18,33]. One group of mostly used machine learning approaches are the deep learning related methods, which include convolutional neural network [47–49], long-term recurrent convolutional networks [50], deep belief networks [51], and self-organizing maps [14]. Although these methods demonstrate great success in capturing the patterns to distinguish the anomalies from the healthy samples, they also have some limitations when being applied to layer-wise anomaly detection. First, these models mostly need to be trained using a relatively large training dataset, which can be quite costly for layer-wise anomaly detection with limited model interpretation. Second, it can be difficult for the deep learning methods to incorporate engineering domain knowledge, such as the layer-wise printing trajectory information, in the modeling and anomaly detection.

In addition, various other methods first leverage feature extraction approaches to extract critical process features from the high-dimensional raw process signals, and subsequently apply various machine learning approaches. The low-dimensional features extracted include melt pool geometric features [52], melt pool boundary related morphological characteristics [13], melt pool surface temperature related features [14,53], tensor decomposition-based features [4,12], auto-encoder-based features [54,55], and various summary statistics of the raw signals [56]. Once the features are extracted, various machine learning methods, such as support vector machines (SVMs) [4,13,32,57], discriminative models [32,56], and random forests [58], have been used for anomaly detection. These methods have demonstrated good performance in anomaly detection for individual observations (e.g., single melt pool images). However, they can be quite cumbersome when being applied to layer-wise anomaly detection for the following two main reasons. First, the thermal distribution of different layers in the same build is continuously varying, and thus it is difficult to establish one benchmark distribution for all the layers in one build. Second, given a complicated component, the thermal behavior also varies as a function of the printing path, which needs to be accounted for in the anomaly detection method.

To fill the above-mentioned gaps, the proposed method aims to extract layer-wise process features that can account for the varying thermal distribution due to different layer change as well as constantly changing printing trajectories. A new in situ layer-wise AM anomaly detection method is proposed by characterizing the morphological dynamics of the melt pools and HAZs which are segmented based on specific temperature ranges. Specifically, for characterizing the morphological dynamics of the melt pools and HAZs, the Wasserstein distance-based optimal transport problem is formulated by leveraging the engineering domain knowledge which is concise and easily interpretable. Subsequently, the WD-based morphological transition metric (MTM) features can be extracted for layer-wise anomaly detection, and a support vector machine-based supervised machine learning framework is leveraged for layer-wise anomaly detection.

3 Methodology

In this section, the proposed methodology is introduced. The melt pool and HAZ in the thermal images are first segmented, and subsequently the new melt pool/HAZ transition metrics are derived by leveraging the Wasserstein distance to quantify the perturbation in a series of melt pools/HAZs' morphologies. The resulted transition metrics are used to extract critical layer-wise features for anomaly detection towards AM part certification. Finally, the supervised learning method is leveraged for layer-wise anomaly detection based on the labeling information generated by post-manufacturing inspection methods, such as XCT. The overall steps of the proposed methodology are illustrated in Fig. 1(*a*), and the data visualization of multiple key steps is shown in Figs. 1(*b*)–1(*e*).

3.1 Melt Pool and Heat Affected Zone Identification.

The thermal images are captured using a pyrometer camera that consists of a temperature measurement at each pixel within the field of view of the camera. To compress the thermal image data without losing useful information for anomaly detection, the widely used concept of heat affected zones is adopted in this paper together with the melt pool to provide more comprehensive information to characterize the observed temperature distribution. For the sake of clarity, the heat affected zone observed in the thermal image is defined as follows.

DEFINITION I: *HAZ*.In each thermal image, the region with temperature readings within a pre-specified temperature range of interests which is lower than the melting temperature (e.g., $\mathcal{R}_2$) of the material is defined as the HAZ.

The melt pool and HAZ's morphologies are primarily governed by two major factors, i.e., the printing path and the AM process stability. Therefore, to quantify the process stability, the printing path induced variability needs to be first removed from the observed thermal history. During the AM fabrication, the instantaneous melt pool orientation is determined by the instantaneous printing

direction, which can be calculated from the printing path in the g-code [16]. Therefore, the image rotation operation is leveraged to align the melt pools with consistent orientation in each layer, as illustrated in Fig. 1(*c*). Let $\mathbf{I}^t \in \mathbb{R}^{r\times c}$ denote the original thermal image collected at time t, which is a matrix with dimension $r\times c$, where r and c are the numbers of rows and columns, respectively. Then, the rotated image can be obtained by Eq. (1):

$$\mathbf{X}^t(\theta) = R(\mathbf{I}^t,\ (\theta - \alpha^t)) \tag{1}$$

where $\mathbf{X}^t(\theta) \in \mathbb{R}^{r\times c}$ denotes the rotated image and the function R denotes the image rotation operation given the pre-specified target orientation θ. Moreover, α^t represents the theoretical instantaneous orientation of the original melt pool ($\mathbf{I}^t$) that can be obtained from the g-code. Furthermore, it is also noted that the selection of θ may consider the major printing orientation in the specific layer to minimize the rotation operations needed. As a result of the rotation operations, the variability of the aligned thermal images (i.e., $\mathbf{X}^t(\theta)$) is mainly determined by the AM process variability.

Subsequently, the melt pools and HAZs are obtained by segmenting $\mathbf{X}^t(\theta)$ based on the corresponding temperature ranges of interests, as presented in Eq. (2).

$$\left(\mathbf{X}_k^t\right)_{a,b} = \begin{cases} \left(\mathbf{X}^t(\theta)\right)_{a,b} & \text{if } \left(\mathbf{X}^t(\theta)\right)_{a,b} \in \mathcal{R}_k \\ 0 & \text{if } \left(\mathbf{X}^t(\theta)\right)_{a,b} \notin \mathcal{R}_k \end{cases}, \quad k = 1, 2 \tag{2}$$

where $\mathbf{X}_1^t \in \mathbb{R}^{r\times c}$ denotes the melt pool region in which $(\cdot)_{a,b}$ representing the entry at the ath row and bth column ($a = 1, 2, \ldots, r$ and $b = 1, 2, \ldots, c$) with $\mathcal{R}_1 = [T_m, +\infty)$ and T_m is the melting temperature of the feedstock material. In addition, $\mathbf{X}_2^t \in \mathbb{R}^{r\times c}$ denotes the HAZ region with $\mathcal{R}_2 = [T_0, T_m)$, and T_0 denotes the lower bound of the pre-specified temperature range of interests.

3.2 Melt Pool and Heat Affected Zone Transition Metrics and Their Properties.

A new transition metric system for both melt pools and HAZs is developed by leveraging the Wasserstein distance formulation. The newly developed transition metrics are introduced as follows;

Definition II: *Global transition metric (GTM)*. The GTM, denoted as $\mathrm{GTM}(\mathbf{X}_k^t,\ \mathbf{X}_k^{t+1})$, quantifies the global mean transition between consecutive melt pools/HAZs and can be thus calculated from the absolute difference between the total summation of the two consecutive melt pools/HAZs, i.e., $\mathbf{X}_k^t$ and $\mathbf{X}_k^{t+1}$, as shown in Eq. (3):

$$\mathrm{GTM}(\mathbf{X}_k^t,\ \mathbf{X}_k^{t+1}) = |1_r^T \mathbf{X}_k^t 1_c - 1_r^T \mathbf{X}_k^{t+1} 1_c| \tag{3}$$

where 1_v represents a $v\times 1$ vector of ones, and thus $1_r^T \mathbf{X}_k^t 1_c$ equals to the sum of all the entries in $\mathbf{X}_k^t$.

Definition III: *Morphological Transition Metric (MTM)*. The MTM focuses on the instantaneous morphological changes between consecutive melt pools/HAZs. After removing the effect of GTM, the normalized melt pools/HAZs can be generated as shown in Eq. (4).

$$\mathbf{Z}_k^t = \mathbf{X}_k^t / (1_r^T \mathbf{X}_k^t 1_c) \tag{4}$$

where $\mathbf{Z}_k^t \in \mathbb{R}^{r\times c}$ denotes the normalized HAZ with kth temperature range $\mathcal{R}_k$. The normalized melt pools/HAZs are used to develop Wasserstein distance based on the optimal transport formulation. To better illustrate the formulation of the optimal transport problem, the terminologies of weight, flow, and work are defined as follows:

Definition IV: *Weight*. The pixel-wise values in the normalized melt pools/HAZ $\mathbf{Z}_k^t$ are defined as the weight, denoted as $w_{k,i}^t$, where i is the one-dimensional index in matrix $\mathbf{Z}_k^t$ and $i = 1, 2, \ldots, rc$. In addition, it denotes the normalized temperature value in the melt pools/HAZs.

Definition V: *Flow*. The flow, denoted as $\mathcal{F}(\mathbf{Z}_k^t, \mathbf{Z}_k^{t+1}) = [f_{ij}^{t,t+1}]_{rc\times rc}$, represents the pixel-wise weight transport from $\mathbf{Z}_k^t$ to $\mathbf{Z}_k^{t+1}$ to achieve the identical normalized melt pools/HAZs, as illustrated in Fig. 2. Here, rc is the total number of pixels in $\mathbf{Z}_k^t$ and $\mathbf{Z}_k^{t+1}$.

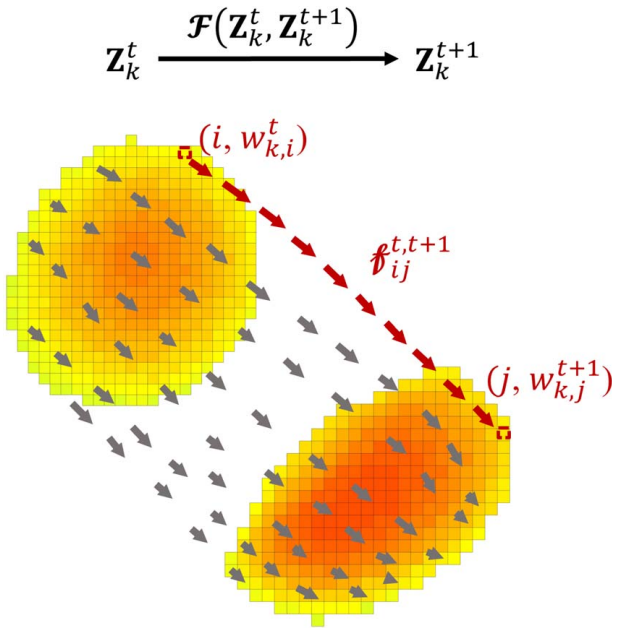

Fig. 2 Visualization of flow $\mathcal{F}(\mathbf{Z}_k^t, \mathbf{Z}_k^{t+1})$, with $f_{ij}^{t,t+1}$ denoting the transport from the *i*th pixel of $\mathbf{Z}_k^t$ to the *j*th pixel of $\mathbf{Z}_k^{t+1}$

Definition VI: *Work*. The work resulted from a feasible flow $\mathcal{F}(\mathbf{Z}_k^t, \mathbf{Z}_k^{t+1})$ in matching $\mathbf{Z}_k^t$ and $\mathbf{Z}_k^{t+1}$ is defined as follows:

$$\mathrm{Work}(\mathcal{F}(\mathbf{Z}_k^t, \mathbf{Z}_k^{t+1})) = \mathrm{tr}(\mathbf{D}(\mathbf{Z}_k^t, \mathbf{Z}_k^{t+1})^T \mathcal{F}(\mathbf{Z}_k^t, \mathbf{Z}_k^{t+1})) \tag{5}$$

where $\mathbf{D}(\mathbf{Z}_k^t, \mathbf{Z}_k^{t+1}) = [||\boldsymbol{u}_{k,i}^t - \boldsymbol{u}_{k,j}^{t+1}||]_{rc\times rc}$ represents the Euclidean distance matrix between individual pixels in $\mathbf{Z}_k^t$ and $\mathbf{Z}_k^{t+1}$, where $\boldsymbol{u}_{k,i}^t \in \mathbb{R}^{1\times 2}$ represents the 2D coordinates of the ith pixel in $\mathbf{Z}_k^t$, and $\boldsymbol{u}_{k,j}^{t+1} \in \mathbb{R}^{1\times 2}$ represents the 2D coordinates of the jth pixel in $\mathbf{Z}_k^{t+1}$ (i and $j = 1, \ldots, rc$). For clarification purpose, a simple demonstrative example with two simple HAZs along with the flow and distance matrix between them is presented in Fig. 3 to illustrate the definition of different matrices in the computation of work.

The MTM is determined by the *optimal* flow from $\mathbf{Z}_k^t$ to $\mathbf{Z}_k^{t+1}$ with the minimum work required to match between the two normalized melt pools/HAZs, which can be obtained by solving the optimization problem as illustrated in Table 2.

The objective function is inspired by the Wasserstein distance, which is the minimum necessary work to transport weight from $\mathbf{Z}_k^t$ to match $\mathbf{Z}_k^{t+1}$. Equation (6) enforces non-negativity requirements to each entry in $\mathcal{F}(\mathbf{Z}_k^t, \mathbf{Z}_k^{t+1})$ (i.e., $f_{ij}^{t,t+1}$). Equations (7) and (8) specify the upper bounds of the total incoming and outgoing flow, respectively. More specifically, the constraint (7) signifies that the total weight in $\mathbf{Z}_k^t$ matched to the jth pixel in $\mathbf{Z}_k^{t+1}$ does not exceed $w_{k,j}^{t+1}$, and similarly the constraint (8) ensures that the total weight in $\mathbf{Z}_k^{t+1}$ matched from the ith pixel in $\mathbf{Z}_k^t$ does not exceed $w_{k,i}^t$. The formulated MTM metric is based on the Wasserstein distance with equal weight distributions, and the weight flows from one distribution to match with the weight of another distribution.

The rationale of using the WD-based metric is first due to its great flexibility in accurately capturing the morphological dynamics in a series of melt pools and HAZs [59]. The extracted GTM and MTM features can be used to characterize the instantaneous change of melt pool and HAZ morphologies which are closely related to AM process stability. Furthermore, the extracted GTM and MTM features also demonstrate the rotation-invariant property, as shown below. This favorable property makes it possible to establish

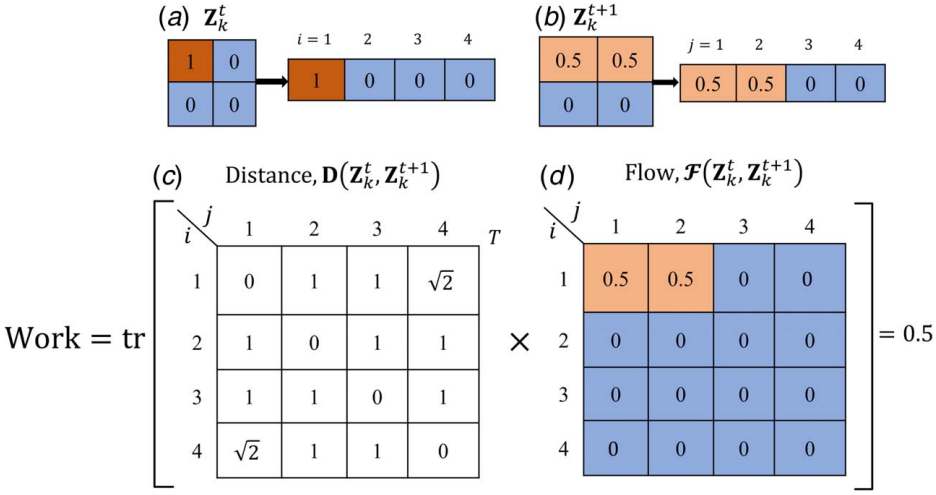

Fig. 3 Visualization of numerical example for computation of work, where (*a*) and (*b*) demonstrate two consecutive normalized HAZs, (*c*) and (*d*) show the distance matrix and flow matrix between two consecutive normalized HAZs, respectively

Table 2 Formulation for optimal flow from $\mathbf{Z}_k^t$ to $\mathbf{Z}_k^{t+1}$

$$\mathrm{MTM}_k^{t,t+1} = \min_{\mathcal{F}(\mathbf{Z}_k^t, \mathbf{Z}_k^{t+1})} \mathrm{Work}(\mathcal{F}(\mathbf{Z}_k^t, \mathbf{Z}_k^{t+1}))$$

Subject to

Non-negativity
$$f_{ij}^{t,t+1} \geq 0 \quad \forall i = 1, \ldots, rc; \quad \forall j = 1, \ldots, rc \tag{6}$$

Upper bounds of flow
$$\sum_{i=1}^{rc} f_{ij}^{t,t+1} = w_{k,j}^{t+1} \quad \forall j = 1, \ldots, rc \tag{7}$$

$$\sum_{j=1}^{rc} f_{ij}^{t,t+1} = w_{k,i}^{t} \quad \forall i = 1, \ldots, rc \tag{8}$$

one benchmark distribution for all the layers with completely different printing trajectories.

PROPOSITION. *Both GTM and MTM are melt pool rotation-invariant metrics*

Proof. For a given pair of $(\mathbf{Z}_k^t, \mathbf{Z}_k^{t+1})$, denote the optimal solution of Table 2 as $\mathcal{F}^*$. Consider the case that $(\mathbf{Z}_k^t, \mathbf{Z}_k^{t+1})$ rotates with an angle α, and denote it as $(\tilde{\mathbf{Z}}_k^t, \tilde{\mathbf{Z}}_k^{t+1}) = (\mathbf{Z}_k^t\mathbf{R}(\alpha), \mathbf{Z}_k^{t+1}\mathbf{R}(\alpha))$, where $\mathbf{R}(\alpha)$ is the rotation matrix. If MTM is melt pool rotation-variant, then $\mathcal{F}^*$ will not be the optimal solution of Table 2 with the input $(\tilde{\mathbf{Z}}_k^t, \tilde{\mathbf{Z}}_k^{t+1})$. Assume the optimal solution is $\tilde{\mathcal{F}}^*$, then we can have

$$\mathrm{Work}(\tilde{\mathcal{F}}^*(\tilde{\mathbf{Z}}_k^t, \tilde{\mathbf{Z}}_k^{t+1})) < \mathrm{Work}(\mathcal{F}^*(\tilde{\mathbf{Z}}_k^t, \tilde{\mathbf{Z}}_k^{t+1})) = \mathrm{Work}(\mathcal{F}^*(\mathbf{Z}_k^t\mathbf{R}(\alpha), \mathbf{Z}_k^{t+1}\mathbf{R}(\alpha)))$$

According to *Definition V*, for a given flow $\mathcal{F}$, $\mathcal{F}(\mathbf{Z}_k^t\mathbf{R}(\alpha), \mathbf{Z}_k^{t+1}\mathbf{R}(\alpha)) = \mathcal{F}(\mathbf{Z}_k^t, \mathbf{Z}_k^{t+1})$. Thus,

$$\mathrm{Work}(\mathcal{F}^*(\mathbf{Z}_k^t\mathbf{R}(\alpha), \mathbf{Z}_k^{t+1}\mathbf{R}(\alpha))) = \mathrm{Work}(\mathcal{F}^*(\mathbf{Z}_k^t, \mathbf{Z}_k^{t+1})) \leq \mathrm{Work}(\tilde{\mathcal{F}}^*(\tilde{\mathbf{Z}}_k^t, \tilde{\mathbf{Z}}_k^{t+1}))$$

which indicates $\mathrm{Work}(\tilde{\mathcal{F}}^*(\tilde{\mathbf{Z}}_k^t, \tilde{\mathbf{Z}}_k^{t+1})) < \mathrm{Work}(\tilde{\mathcal{F}}^*(\tilde{\mathbf{Z}}_k^t, \tilde{\mathbf{Z}}_k^{t+1}))$. This, however, is impossible. Thus, based on the proof by contradiction, MTM is melt pool rotation-invariant.

Similar proof can be applied to GTM. This rotation-invariant property for the proposed GTM and MTM metrics ensures that layers with different major printing orientations can share the same benchmark for AM layer-wise certification.

To find the MTM feature values, the optimization problem in Table 2 can be solved effectively by an efficient numerical algorithm (i.e., Algorithm 2M) proposed in Ref. [60], which is a cascadic multilevel primal-dual based algorithm. In this algorithm, the WD metrics are iteratively updated, where the coarse grids are used as the initial solution for solving the problem using the finer grids. This iterative mechanism significantly reduces the computational time to find the optimal solution. More specifically, the normalized melt pools/HAZs, denoted as $\mathbf{Z}_k^t$ and $\mathbf{Z}_k^{t+1}$ in Table 2, are corresponding to two distributions between which to calculate the WD metrics in Ref. [60], and the feature $\mathrm{MTM}_k^{t,t+1}$ in our problem is corresponding to the optimal transport between $\mathbf{Z}_k^t$ and $\mathbf{Z}_k^{t+1}$. Once defining the initiation parameters including grid step size, number of grid levels, and the sequence of stopping tolerance, the optimal solution is computed following an iterative approach with different sizes of the grids. The computational cost of this algorithm in the proposed framework will be examined in the case study (Sec. 4). ■

3.3 Layer-Wise Feature Extraction for Process Anomaly Detection. Based on the new transition metrics developed, the layer-wise features can be extracted. Since the transition metrics characterize the morphological dynamics of the melt pools and HAZs, their values should be very small when the AM process is healthy, and relatively large when there is a process anomaly. As a result, the maximum values of both features are used to quantify the morphology series' most extreme change for layer-wise anomaly detection. This is similar to the idea of using group control chart in statistical quality control in order to control the type I error rate when simultaneously monitoring multiple data streams [61,62]. Therefore, the maximum of all the $\mathrm{GTM}(\mathbf{X}_k^t, \mathbf{X}_k^{t+1})$ values is captured from each layer, and thus the

relevant layer-wise feature ℓGTM_l^k can be calculated in Eq. (9):

$$\ell\text{GTM}_l^k = \max_{t\in\mathcal{T}_l}\{\text{GTM}(\mathbf{X}_k^t,\ \mathbf{X}_k^{t+1})\}\ (k=1,2) \tag{9}$$

where $\mathcal{T}_l$ represents the set of time stamps within the build of the lth layer.

In addition, the layer-wise melt pools/HAZs morphological dynamics can be characterized by the maximum of the multiple MTM values extracted from the consecutive melt pools/HAZs in the same layer, denoted as ℓMTM_l^k, as calculated in Eq. (10):

$$\ell\text{MTM}_l^k = \max_{t\in\mathcal{T}_l}\{\text{MTM}_k^{t,t+1}\}\quad (k=1,2) \tag{10}$$

where $\mathcal{T}_l$ represents the set of time stamps that are within the build of the lth layer.

3.4 In Situ Layer-Wise Anomaly Detection Based on Supervised Learning. Supervised learning algorithms can be used to establish a distinction between healthy and unhealthy layers based on the layer-wise features extracted. The post-manufacturing XCT scanning can be used to obtain structural quality information of each layer, providing the ground truth information to the data set. For layer-wise anomaly detection, one layer is labeled as abnormal if there is at least one porosity observed. It is worth noting that all different machine learning methods can be used to detect layer-wise anomalies. The SVM technique is adopted in this work because of the flexibility it can offer in learning the decision boundaries by varying kernel functions. The SVM classifier can be trained by finding the hyperplane that best separates all data points of distinct classes using a training data set with labeling information, and the complexity of the hyperplane can be determined through cross validation [63]. In summary, the newly proposed in situ layer-wise anomaly detection algorithm is illustrated in Table 3.

4 Case Study

In this section, the proposed in situ layer-wise anomaly detection method is validated based on the data collected from two specimens using the DED process, which is one of the most common techniques to perform powder-based DED.

Table 3 The proposed algorithm for in situ layer-wise anomaly detection for DED processes

Input: Layer-wise original thermal images $\{\mathbf{I}^t \in \mathbb{R}^{r\times c}\}$, where $t \in \mathcal{T}_l$ and $\mathcal{T}_l$ represent the set of time stamps that are within the build of the lth layer.
Output: In situ layer-wise anomaly detection.

Algorithm:
Step 1 (Melt pool and HAZ identification):
1.1: Rotate original thermal images as $\mathbf{X}^t(\theta) \in \mathbb{R}^{r\times c}$ based on Eq. (1).
1.2: Generate melt pools/HAZs by segmenting $\mathbf{X}^t(\theta)$ as $\mathbf{X}_k^t \in \mathbb{R}^{r\times c}$ using Eq. (2) ($k=1, 2$).
Step 2 (Melt pool and HAZ transition metrics calculation):
2.1: Calculate the $\text{GTM}(\mathbf{X}_k^t,\ \mathbf{X}_k^{t+1})$ values based on Eq. (3).
2.2: Calculate the $\text{MTM}_k^{t,t+1}$ values by solving the optimization problem in Table 2.
Step 3 (Layer-wise feature extraction):
3.1: Compute the ℓGTM_l^k value using Eq. (9).
3.2: Compute the ℓMTM_l^k value using Eq. (10).
Step 4 (Supervised learning for in situ layer-wise anomaly detection):
4.1: Train the SVM model using ℓGTM_l^k, ℓMTM_l^k ($k=1, 2$) and layer-wise binary response variable of training dataset.
4.2: Assess the average performance of the model based on the test data set.

Table 4 Process parameters for fabricating the specimens

Parameters	Thin wall	Cylinder
Scan speed	30 in./min	40 in./min
Powder feed rate	4 rpm	3 rpm
Hatch spacing	0.02 in.	0.02 in.
Power	300 W	300 W
Layer thickness	0.02 in.	0.015 in.
Nozzle diameter	0.035 in.	0.035 in.
Number of thermal images captured	1557	2827
Number of layers	60	69
Number of abnormal layers	26	58
Infill pattern	–	Unidirectional (180 deg rotation between layers)

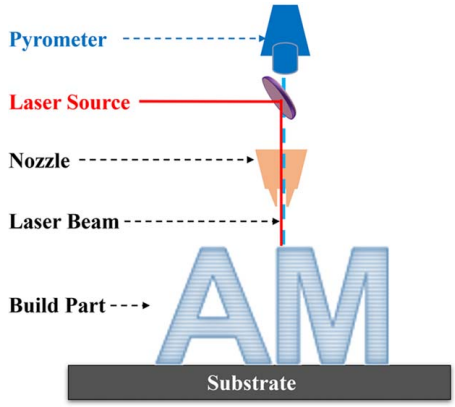

Fig. 4 Experimental setup of the DED process equipped with the coaxial pyrometer

4.1 Experimental Setup. The machine used for data collection was the LENS 750 machine manufactured by OPTOMEC, and the machine is equipped with the 1 kW Nd:YAG laser [16]. To evaluate the robustness of the proposed method, two specimens with different geometries (i.e., one thin wall and one cylindrical shaped part) were fabricated using the Ti–6Al–4V powder as the feedstock material. The process parameters used for both specimen fabrication are listed in Table 4 [16].

For process data collection, the dual-wavelength coaxial pyrometer (Stratonics, Inc.) captures the temperature distribution from the top view of melt pool. The key benefit of using the pyrometer camera is that the image data collected demonstrate reduced motion blur, as it has a specific exposure period (2.0274 ms) with the nominal image collection rate of approximately 6.4 Hz. A brief sketch of the experimental setup with the sensor positioning is illustrated in Fig. 4.

Each observed thermal image is in the form of a 752×480 matrix, which consists of the temperature values at each pixel within the range of 1000–2500 °C. During the thin wall fabrication, the captured melt pools in each layer represent identical orientation, due to its unidirectional printing path. However, for the cylindrical specimen, the layer-wise melt pools demonstrate varying orientations due to the complex printing paths. Furthermore, using the XCT inspection (Skyscan 1172) technology, the porosities in the printed specimens were characterized, and thus the layer-wise process data were labeled using the porosity characterization results [14]. All the layers that include at least one pore with diameter larger than 0.05 mm were labeled as unhealthy [3].

4.2 Benchmark Method Selection. Two benchmark methods of layer-wise AM process anomaly detection are selected to

compare with the proposed method. The first benchmark method was the layer-wise anomaly detection model proposed by Seifi et al. [4], which leveraged multi-linear principal component analysis (MPCA). In this approach, the MPCA algorithm was used for dimensionality reduction for each single thermal image, and then the volume of the convex hull formed by the extracted multi-linear principal components from each layer was employed as a layer-wise process feature for anomaly detection. In addition, the maximum norm value of the residual from the MPCA modeling within a layer was used as a secondary layer-wise feature during classification for anomaly detection. The effectiveness of this benchmark method was validated by comparing with the traditional machine learning driven anomaly detection approaches.

More recently, in situ layer-wise certification of direct laser deposition process based on image series analysis was proposed by Esfahani et al. [16]. This method leverages the image registration technique to characterize the thermal history dynamics in the layer-wise thermal images. Moreover, the Gaussian process (GP) models were employed to characterize the unexplained variation component by the image registration operation. The effectiveness of this benchmark method was validated by comparing with the approach proposed by Seifi et al. [4].

4.3 Results and Discussions. In this study, to compare the effectiveness of the proposed and the benchmark methods, both thin wall and cylinder data set were randomly split into the training layer set (80%) and testing layer set (20%), and 200 replications of this evaluation were performed to assess the average performance. Basically, using the training layer set, the Gaussian SVM classification model can be trained when the GTM and MTM features have been defined, which can then be used to predict the labels of newly observed layers. Specifically, the classifier is fed a vector of response labels (0 for healthy, 1 for unhealthy) and a matrix of four predictors: the GTM and MTM extracted from the melt pool and tail region, respectively. The features of GTM and MTM are associated with the segmented melt pools/HAZs of thermal images, and the selection of temperature range of interests to segment the HAZ affects the extracted features and the prediction accuracy. In this case, the melt pool regions were segmented based on the melting point of the feedstock material and above, i.e., $\mathcal{R}_1 = [1636, +\infty)$, and the HAZs were segmented considering some specific temperature to the melting point of the feedstock material, i.e., $\mathcal{R}_2 = [T_0, 1636)$, which can define as the tail region of the melt pool.

The lower bound T_0 of the tail region temperature range can be considered as the tuning parameter in the proposed approach. By tuning the value of T_0, the effect of different temperature ranges of interests on the extracted features in both the thin wall and cylindrical specimen can be depicted as shown in Fig. 5. It can be observed that different values of T_0 lead to different distinguishability between the healthy and unhealthy layers for both specimens, demonstrating the necessity of parameter tuning for the lower bound temperature T_0.

Four key performance metrics (i.e., accuracy, recall, precision, and F-score) are used to evaluate both methods given the same data set. The four metrics are commonly used in evaluating supervised learning methods [4,13,16] and are defined as follows:

$$\text{Accuracy} = \frac{\text{TP} + \text{TN}}{\text{TP} + \text{FP} + \text{TN} + \text{FN}} \tag{11}$$

$$\text{Recall} = \frac{\text{TP}}{\text{TP} + \text{FN}} \tag{12}$$

$$\text{Precision} = \frac{\text{TP}}{\text{TP} + \text{FP}} \tag{13}$$

$$F - \text{score} = 2 \times \frac{\text{Precision} \times \text{Recall}}{\text{Precision} + \text{Recall}} \tag{14}$$

where TP, TN, FN, and FP denote true-positive, true-negative, false-negative, and false-positive, respectively, which are the key elements in confusion matrix. More specifically, true-positive (TP) denotes accurate prediction of unhealthy layers, whereas true-negative (TN) represents the layers accurately predicted as healthy. In addition, false-negative (FN) denotes the unhealthy layers predicted inaccurately as healthy, while false-positive (FP) represents the inaccurate prediction of healthy layers as unhealthy. Moreover, the F-score represents the harmonic mean of precision and recall, which is used in this paper as the key indicator for performance comparison.

As mentioned above, the tuning parameter affects the extracted features and subsequently the prediction results. Therefore, by tuning the temperature range of the tail region, the performance metrics are listed as shown in Table 5, where $\mathcal{R}_1$ is always fixed and $\mathcal{R}_2$ changes as the T_0 value is tuned. From Table 5, it is observed that in the case of thin wall, $T_0 = 1000\,^{\circ}\text{C}$ (bolded) provides the highest F-score value. Furthermore, in the case of cylinder, the F-score value shows the best results when $T_0 = 1400\,^{\circ}\text{C}$ (bolded).

The performance metrics of the proposed and benchmark methods are summarized in Table 6. Furthermore, a number of sample size values were explored to examine the effects of the

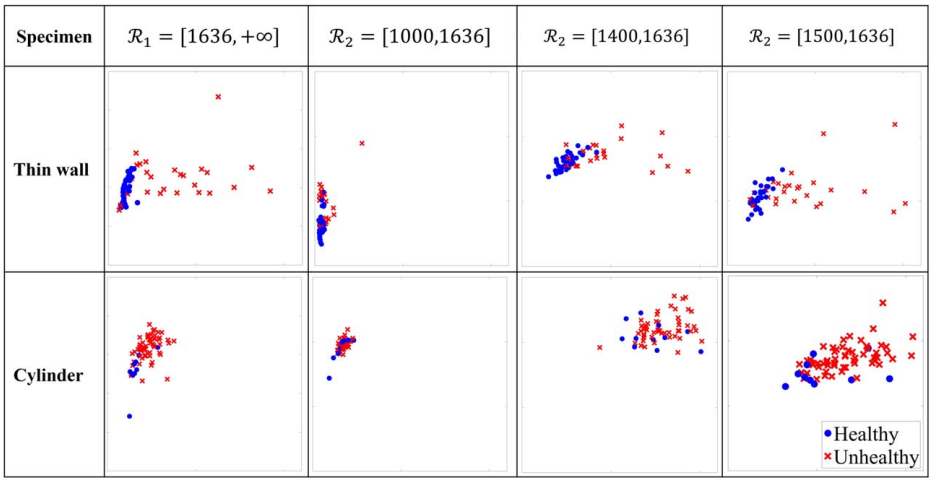

Fig. 5 Extracted layer-wise features of ℓGTM ($x-$axis) versus ℓMTM ($y-$axis) for different temperature ranges of interest, where the dots denote healthy layers and the crosses denote unhealthy layers

Table 5 Performance comparison by tuning temperature range of interest (R_2)

Specimen	Metric	T_0 1000 °C	1100 °C	1200 °C	1300 °C	1400 °C	1500 °C
Thin wall	Accuracy	**96.00%**	95.95%	96.65%	94.45%	88.35%	92.95%
	Precision	**96.80%**	97.70%	97.35%	92.42%	87.96%	98.03%
	Recall	**99.82%**	93.77%	94.04%	95.64%	89.37%	86.11%
	F-score	**96.04%**	95.10%	94.85%	93.18%	87.42%	90.33%
Cylinder	Accuracy	84.73%	84.09%	80.73%	83.00%	**86.05%**	83.00%
	Precision	82.50%	84.27%	81.55%	81.68%	**83.27%**	82.24%
	Recall	97.91%	97.88%	96.83%	99.81%	**100.00%**	98.31%
	F-score	90.07%	90.27%	88.13%	89.52%	**90.67%**	89.23%

Table 6 Performance comparison between the proposed and benchmark method

Specimen	Metric	Proposed method	Seifi et al. [4]	Esfahani et al. [16] $s=50$	$s=100$	$s=150$	$s=200$	$s=300$	$s=400$
Thin wall	Accuracy	96.38%	94.67%	93.54%	93.17%	93.00%	93.92%	93.12%	93.25%
	Precision	97.36%	95.91%	94.75%	91.88%	91.63%	93.64%	91.85%	92.50%
	Recall	94.47%	90.98%	91.20%	93.58%	93.58%	93.68%	93.68%	93.58%
	F-score	95.34%	93.24%	92.36%	92.10%	91.97%	93.06%	92.10%	92.38%
Cylinder	Accuracy	85.07%	73.60%	84.29%	84.21%	83.96%	83.93%	83.11%	83.21%
	Precision	84.71%	81.46%	84.97%	84.96%	84.86%	84.85%	84.76%	84.78%
	Recall	100.00%	88.05%	99.18%	98.94%	98.72%	98.68%	97.76%	97.89%
	F-score	91.56%	84.12%	91.26%	91.18%	91.02%	91.00%	90.52%	90.59%

sample size used in fitting the GP model for the error matrix in Ref. [16] for a fair comparison. When comparing the *F*-score, it is observed that the proposed method outperforms both benchmark methods for the thin wall specimen. Moreover, for the cylindrical specimen, the proposed method outperforms Seifi et al.'s [4] in all four metrics and demonstrates comparable (or slightly better) Fscore results with Esfahani et al. [16]. The good performance of the proposed method is mainly due to its joint consideration of the layer-wise melt pools/HAZs morphological dynamics. In addition, given the robustness in the performance of the proposed method in both thin wall and cylindrical specimens, the proposed method can be applied for in situ layer-wise anomaly detection for intricate shaped parts.

There are three possible reasons for the classification errors observed in the case study. First, the discrete data sampling of the pyrometer camera may potentially lead to a lot of missing data in the thermal data collection, resulting in missing defect inducing process information. Second, the characterization of XCT scanning may be subject to noise and error, leading to occasional labeling errors in the data set. Third, the proposed in situ layer-wise anomaly detection approach ignores the impacts of re-melting between consecutive layers and adjacent tracks, which may eliminate some porosities formed in the preceding layer/track during subsequent layer/track deposition.

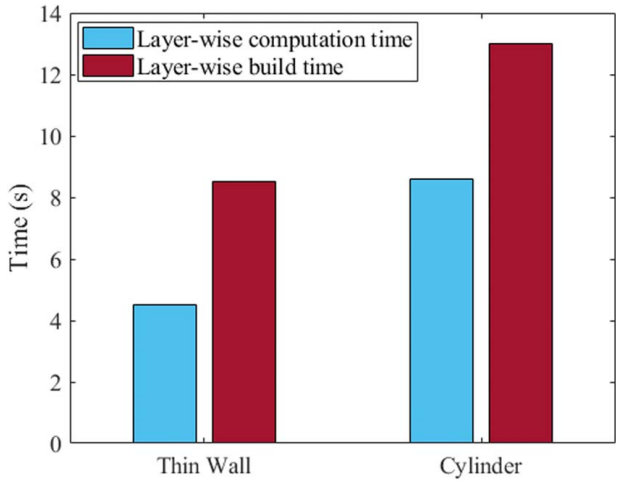

Fig. 6 Layer-wise average computation time of the proposed method

The average computational efficiency of the proposed method is illustrated in Fig. 6, where the average computation time and the average build time for each layer are compared for both specimens. The processor used to implement the proposed method was Intel® Core™ Processor i7–7700 CPU at 3.60 GHz. It is worth noting that the average computation for the proposed method takes significantly shorter time than its corresponding layer-wise build time for both thin wall and cylinder specimen. As a result, the proposed method can facilitate layer-wise AM certification in real time, potentially enabling real-time process control for quality improvement.

5 Conclusion and Future Work

The quality issues are the major barriers for wider and sustainable industrial adoption of the AM technology, and there is a need of reliable techniques to detect quality issues (i.e., porosity, mini cracks, lack of fusion, etc.) in AM processes. Different approaches like FEMs are used to characterize the anomaly based on thermomechanical relationship, but they cannot realistically capture process uncertainty. These limitations are addressed by the data-driven approaches where usually the individual thermal images of the melt pools are used for local anomaly prediction. Few approaches are proposed for layer-wise anomaly detection, and the extracted features cannot explicitly characterize melt pool/HAZ morphological dynamics.

This paper proposes a novel formulation of melt pools and HAZs morphological dynamics through which the new melt pool/HAZ transition metrics are derived. Furthermore, novel layer-wise process key features are derived from the characterization of melt

pools/HAZs morphological dynamics for AM layer-wise anomaly detection. Specifically, morphological transition between consecutive melt pools/HAZs along with the global temperature shift are extracted as the novel features. Based on the extracted layer-wise features, the SVM classification approach is used for in situ layer-wise anomaly detection. The specimens of a thin wall and a cylinder were fabricated using the DED process to validate the proposed methodology. The anomaly detection accuracy of the proposed model is reasonably high and outperforms both benchmark methods, which are both state-of-the-art AM layer-wise anomaly detection methods.

For future research, a couple of interesting topics remain open. First, the inter-layer and inter-track dependence during fabrication can be characterized to quantify the re-melting effect between the adjacent layers/tracks. Second, a part certification framework can be established to quantify the size and severity of the defects and their impact to the part functionality. Finally, layer-wise process control algorithms can be used in conjunction with the in situ monitoring scheme to adjust process parameters for quality improvement of the AM parts.

Acknowledgment

This work was partially sponsored by the National Science Foundation (No. CMMI-2046515).

Conflict of Interest

There are no conflicts of interest.

Data Availability Statement

The datasets generated and supporting the findings of this article are obtainable from the corresponding author upon reasonable request.

References

[1] Shamsaei, N., Yadollahi, A., Bian, L., and Thompson, S. M., 2015, "An Overview of Direct Laser Deposition for Additive Manufacturing; Part II: Mechanical Behavior, Process Parameter Optimization and Control," Addit. Manuf., **8**, pp. 12–35.
[2] Liu, C., Tian, W., and Kan, C., 2022, "When AI Meets Additive Manufacturing: Challenges and Emerging Opportunities for Human-Centered Products Development," J. Manuf. Syst.
[3] Tian, Q., Guo, S., Melder, E., Bian, L., and Guo, W., 2021, "Deep Learning-Based Data Fusion Method for In-Situ Porosity Detection in Laser-Based Additive Manufacturing," ASME J. Manuf. Sci. Eng., **143**(4), p. 041011.
[4] Seifi, S. H., Tian, W., Doude, H., Tschopp, M. A., and Bian, L., 2019, "Layer-Wise Modeling and Anomaly Detection for Laser-Based Additive Manufacturing," ASME J. Manuf. Sci. Eng., **141**(8), p. 081013.
[5] Jurrens, K., Migler, K., Ricker, R., Pei, Z., Schmid, S., Love, L., Resnick, R., and Vorvolakos, K., 2013, "Measurement Science Roadmap for Metal-Based Additive Manufacturing," NIST, Gaithersburg, MD.
[6] Bae, C.-J., Diggs, A. B., and Ramachandran, A., 2018, *Additive Manufacturing Materials: Processes, Quantifications and Applications*, Elsevier, Oxford, UK, pp. 181–213.
[7] Chen, Z., Han, C., Gao, M., Kandukuri, S. Y., and Zhou, K., 2022, "A Review on Qualification and Certification for Metal Additive Manufacturing," Virtual Phys. Prototyp., **17**(2), pp. 382–405.
[8] AIA, 2020, "Report: Recommended Guidance for Certification of AM Components," pp. 0–39
[9] L. R. & T. Ltd, 2020, "Guidance Notes for Additive Manufacturing of Metallic Parts," Additive Manufacturing.
[10] Romano, J., Ladani, L., and Sadowski, M., 2015, "Thermal Modeling of Laser Based Additive Manufacturing Processes Within Common Materials," Procedia Manuf., **1**, pp. 238–250.
[11] Tian, H., Chen, X., Yan, Z., Zhi, X., Yang, Q., and Yuan, Z., 2019, "Finite-Element Simulation of Melt Pool Geometry and Dilution Ratio During Laser Cladding," Appl. Phys. A Mater. Sci. Process., **125**(7), pp. 1–9.
[12] Khanzadeh, M., Tian, W., Yadollahi, A., Doude, H. R., Tschopp, M. A., and Bian, L., 2018, "Dual Process Monitoring of Metal-Based Additive Manufacturing Using Tensor Decomposition of Thermal Image Streams," Addit. Manuf., **23**, pp. 443–456.
[13] Khanzadeh, M., Chowdhury, S., Marufuzzaman, M., Tschopp, M. A., and Bian, L., 2018, "Porosity Prediction: Supervised-Learning of Thermal History for Direct Laser Deposition," J. Manuf. Syst., **47**, pp. 69–82.
[14] Khanzadeh, M., Chowdhury, S., Tschopp, M. A., Doude, H. R., Marufuzzaman, M., and Bian, L., 2019, "In-Situ Monitoring of Melt Pool Images for Porosity Prediction in Directed Energy Deposition Processes," IISE Trans., **51**(5), pp. 437–455.
[15] Grasso, M., Demir, A. G., Previtali, B., and Colosimo, B. M., 2018, "In Situ Monitoring of Selective Laser Melting of Zinc Powder Via Infrared Imaging of the Process Plume," Robot. Comput. Integr. Manuf., **49**, pp. 229–239.
[16] Esfahani, M. N., Bappy, M., Bian, L., and Tian, W., 2022, "In-Situ Layer-Wise Certification for Direct Laser Deposition Processes Based on Thermal Image Series Analysis," J. Manuf. Process, **75**, pp. 895–902.
[17] Scime, L., and Beuth, J., 2019, "Melt Pool Geometry and Morphology Variability for the Inconel 718 Alloy in a Laser Powder Bed Fusion Additive Manufacturing Process," Addit. Manuf., **29**, p. 100830.
[18] Wang, C., Tan, X. P., Tor, S. B., and Lim, C. S., 2020, "Machine Learning in Additive Manufacturing: State-of-the-Art and Perspectives," Addit. Manuf., **36**, p. 101538.
[19] Naresh, K., Khan, K. A., Umer, R., and Cantwell, W. J., 2020, "The Use of X-Ray Computed Tomography for Design and Process Modeling of Aerospace Composites: A Review," Mater. Des., **190**, p. 108553.
[20] Vora, H. D., and Sanyal, S., 2020, "A Comprehensive Review: Metrology in Additive Manufacturing and 3D Printing Technology," Prog. Addit. Manuf., **5**(4), pp. 319–353.
[21] Haleem, A., and Javaid, M., 2018, "Role of CT and MRI in the Design and Development of Orthopaedic Model Using Additive Manufacturing," J. Clin. Orthop. Trauma, **9**(3), pp. 213–217.
[22] Kim, C., Yin, H., Shmatok, A., Prorok, B. C., Lou, X., and Matlack, K. H., 2021, "Ultrasonic Nondestructive Evaluation of Laser Powder Bed Fusion 316L Stainless Steel," Addit. Manuf., **38**, p. 101800.
[23] Ye, Z., Liu, C., Tian, W., and Kan, C., 2021, "In-Situ Point Cloud Fusion for Layer-Wise Monitoring of Additive Manufacturing," J. Manuf. Syst., **61**, pp. 210–222.
[24] Liu, C., Wang, R. R., Ho, I., Kong, Z. J., Williams, C., Babu, S., and Joslin, C., 2022, "Toward Online Layer-Wise Surface Morphology Measurement in Additive Manufacturing Using a Deep Learning-Based Approach," J. Intell. Manuf., in press, pp. 1–17.
[25] Lifton, J., and Liu, T., 2021, "An Adaptive Thresholding Algorithm for Porosity Measurement of Additively Manufactured Metal Test Samples Via X-Ray Computed Tomography," Addit. Manuf., **39**, p. 101899.
[26] Pokorný, P., Václav, Š., Petru, J., and Kritikos, M., 2021, "Porosity Analysis of Additive Manufactured Parts Using CAQ Technology," Materials (Basel), **14**(5), pp. 1–14.
[27] Gobert, C., Kudzal, A., Sietins, J., Mock, C., Sun, J., and McWilliams, B., 2020, "Porosity Segmentation in X-Ray Computed Tomography Scans of Metal Additively Manufactured Specimens With Machine Learning," Addit. Manuf., **36**, p. 101460.
[28] Soltani, F., Goueygou, M., Lafhaj, Z., and Piwakowski, B., 2013, "Relationship Between Ultrasonic Rayleigh Wave Propagation and Capillary Porosity in Cement Paste With Variable Water Content," NDT E Int., **54**, pp. 75–83.
[29] Karthik, N. V., Gu, H., Pal, D., Starr, T., and Stucker, B., 2013, "High Frequency Ultrasonic Non Destructive Evaluation of Additively Manufactured Components," 24th International SFF Symposium—An Additive Manufacturing Conference SFF, University of Texas at Austin, Aug. 16.
[30] Khanzadeh, M., Dantin, M., Tian, W., Priddy, M. W., Doude, H., and Bian, L., 2022, "Fast Prediction of Thermal Data Stream for Direct Laser Deposition Processes Using Network-Based Tensor Regression," ASME J. Manuf. Sci. Eng., **144**(4), p. 041004.
[31] Xiyue, Z., Aidin, I., Mojtaba, K., Farhad, I., and Linkan, B., 2021, "Automated Anomaly Detection of Laser-Based Additive Manufacturing Using Melt Pool Sparse Representation and Unsupervised Learning," 2021 International Solid Freeform Fabrication Symposium, University of Texas at Austin, Aug. 2-4.
[32] Mahmoudi, M., Ezzat, A. A., and Elwany, A., 2019, "Layerwise Anomaly Detection in Laser Powder-Bed Fusion Metal Additive Manufacturing," ASME J. Manuf. Sci. Eng., **141**(3), p. 031002.
[33] Grasso, M., and Colosimo, B. M., 2017, "Process Defects and In Situ Monitoring Methods in Metal Powder Bed Fusion: A Review," Meas. Sci. Technol., **28**(4), pp. 1–40.
[34] Mitchell, J. A., Ivanoff, T. A., Dagel, D., Madison, J. D., and Jared, B., 2020, "Linking Pyrometry to Porosity in Additively Manufactured Metals," Addit. Manuf., **31**, p. 100946.
[35] Scime, L., and Beuth, J., 2018, "A Multi-Scale Convolutional Neural Network for Autonomous Anomaly Detection and Classification in a Laser Powder Bed Fusion Additive Manufacturing Process," Addit. Manuf., **24**, pp. 273–286.
[36] Tian, Q., Guo, S., and Guo, Y., 2020, "A Physics-Driven Deep Learning Model for Process-Porosity Causal Relationship and Porosity Prediction With Interpretability in Laser Metal Deposition," CIRP Ann., **69**(1), pp. 205–208.
[37] Reisch, R., Hauser, T., Lutz, B., Pantano, M., Kamps, T., and Knoll, A., 2020, "Distance-Based Multivariate Anomaly Detection in Wire Arc Additive Manufacturing," Proceedings—19th IEEE International Conference on Machine Learning & Applications (ICMLA 2020), Miami, FL, Dec. 14–17.
[38] Liu, C., Law, A. C. C., Roberson, D., and Kong, Z. J., 2019, "Image Analysis-Based Closed Loop Quality Control for Additive Manufacturing With Fused Filament Fabrication," J. Manuf. Syst., **51**, pp. 75–86.

[39] Al Mamun, A., Liu, C., Kan, C., and Tian, W., 2022, "Securing Cyber-Physical Additive Manufacturing Systems by In-Situ Process Authentication Using Streamline Video Analysis," J. Manuf. Syst., **62**, pp. 429–440.
[40] Liu, C., Kong, Z., Babu, S., Joslin, C., and Ferguson, J., 2021, "An Integrated Manifold Learning Approach for High-Dimensional Data Feature Extractions and Its Applications to Online Process Monitoring of Additive Manufacturing," IISE Trans., **53**(11), pp. 1215–1230.
[41] Yan, H., Grasso, M., Paynabar, K., and Colosimo, B. M., 2020, "Real-Time Detection of Clustered Events in Video-Imaging Data With Applications to Additive Manufacturing," IISE Trans., **54**(5), pp. 464–480.
[42] Colosimo, B. M., and Grasso, M., 2018, "Spatially Weighted PCA for Monitoring Video Image Data With Application to Additive Manufacturing," J. Qual. Technol., **50**(4), pp. 391–417.
[43] Chen, L., Yao, X., Xu, P., Moon, S. K., and Bi, G., 2021, "Rapid Surface Defect Identification for Additive Manufacturing With In-Situ Point Cloud Processing and Machine Learning," Virtual Phys. Prototyp., **16**(1), pp. 50–67.
[44] Li, R., Jin, M., and Paquit, V. C., 2021, "Geometrical Defect Detection for Additive Manufacturing With Machine Learning Models," Mater. Des., **206**, p. 109726.
[45] Tootooni, M. S., Dsouza, A., Donovan, R., Rao, P. K., Kong, Z. J., and Borgesen, P., 2017, "Classifying the Dimensional Variation in Additive Manufactured Parts From Laser-Scanned Three-Dimensional Point Cloud Data Using Machine Learning Approaches," ASME J. Manuf. Sci. Eng., **139**(9), p. 091005
[46] Jaklič, A., Erič, M., Mihajlović, I., Stopinšek, Ž., and Solina, F., 2015, "Volumetric Models From 3D Point Clouds: The Case Study of Sarcophagi Cargo From a 2nd/3rd Century AD Roman Shipwreck Near Sutivan on Island Brač, Croatia," J. Archaeol. Sci., **62**, pp. 143–152.
[47] Yuan, B., Giera, B., Guss, G., Matthews, M., and McMains, S., 2019, "Semi-Supervised Convolutional Neural Networks for In-Situ Video Monitoring of Selective Laser Melting," Proceedings—2019 IEEE Winter Conference on Applications of Computer Vision, WACV 2019, Waikoloa Village, HI, Jan. 7–11.
[48] Francis, J., and Bian, L., 2019, "Deep Learning for Distortion Prediction in Laser-Based Additive Manufacturing Using Big Data," Manuf. Lett., **20**, pp. 10–14.
[49] Seifi, S. H., Yadollahi, A., Tian, W., Doude, H., Hammond, V. H., and Bian, L., 2021, "In Situ Nondestructive Fatigue-Life Prediction of Additive Manufactured Parts by Establishing a Process–Defect–Property Relationship," Adv. Intell. Syst., **3**(12), p. 2000268.
[50] Tian, Q., Guo, S., Melder, E., Bian, L., and Guo, W., 2021, "Deep Learning-Based Data Fusion Method for In Situ Porosity Detection in Laser-Based Additive Manufacturing," ASME J. Manuf. Sci. Eng., **143**(4), p. 041011.
[51] Ye, D., Hsi Fuh, J. Y., Zhang, Y., Hong, G. S., and Zhu, K., 2018, "In Situ Monitoring of Selective Laser Melting Using Plume and Spatter Signatures by Deep Belief Networks," ISA Trans., **81**, pp. 96–104.
[52] Yang, Z., Lu, Y., Yeung, H., and Krishnamurty, S., 2019, "Investigation of Deep Learning for Real-Time Melt Pool Classification in Additive Manufacturing," 2019 IEEE 15th International Conference on Automation Science and Engineering (CASE), Vancouver, BC, Canada, Aug. 22–26.
[53] Feng, W., Mao, Z., Yang, Y., Ma, H., Zhao, K., Qi, C., Hao, C., Liu, Z., Xie, H., and Liu, S., 2022, "Online Defect Detection Method and System Based on Similarity of the Temperature Field in the Melt Pool," Addit. Manuf., **54**, p. 102760.
[54] Shi, Z., Al Mamun, A., Kan, C., Tian, W., and Liu, C., 2022, "An LSTM-Autoencoder Based Online Side Channel Monitoring Approach for Cyber-Physical Attack Detection in Additive Manufacturing," J. Intell. Manuf., in press, pp. 1–17.
[55] Shi, Z., Mandal, S., Harimkar, S., and Liu, C., 2021, "Surface Morphology Analysis Using Convolutional Autoencoder in Additive Manufacturing With Laser Engineered Net Shaping," Procedia Manuf., **53**, pp. 16–23.
[56] Gaja, H., and Liou, F., 2018, "Defect Classification of Laser Metal Deposition Using Logistic Regression and Artificial Neural Networks for Pattern Recognition," Int. J. Adv. Manuf. Technol., **94**(1–4), pp. 315–326.
[57] Imani, F., Gaikwad, A., Montazeri, M., Rao, P., Yang, H., and Reutzel, E., 2018, "Process Mapping and In-Process Monitoring of Porosity in Laser Powder Bed Fusion Using Layerwise Optical Imaging," ASME J. Manuf. Sci. Eng., **140**(10), p. 101009.
[58] García-Moreno, A. I., Alvarado-Orozco, J. M., Ibarra-Medina, J., and Martínez-Franco, E., 2020, "Image-Based Porosity Classification in Al-Alloys by Laser Metal Deposition Using Random Forests," Int. J. Adv. Manuf. Technol., **110**(9–10), pp. 2827–2845.
[59] Lee, W., Li, W., Lin, B., and Monod, A., 2021, "Tropical Optimal Transport and Wasserstein Distances," Inf. Geom., pp. 1–13.
[60] Liu, J., Yin, W., Li, W., and Chow, Y. T., 2018, "Multilevel Optimal Transport: A Fast Approximation of Wasserstein-1 Distances," arXiv.
[61] Tian, W., Jin, R., Huang, T., and Camelio, J. A., 2017, "Statistical Process Control for Multistage Processes With Non-Repeating Cyclic Profiles," IISE Trans., **49**(3), pp. 320–331.
[62] Xiang, L., and Tsung, F., 2008, "Statistical Monitoring of Multi-Stage Processes Based on Engineering Models," IIE Trans., **40**(10), pp. 957–970.
[63] Friedman, J., Hastie, T., and Tibshirani, R., 2001, *The Elements of Statistical Learning*, Springer, New York.